Geochemical characterization using geophysical data and Markov Chain Monte Carlo methods: A case study at the South Oyster bacterial transport site in Virginia

Jinsong Chen,[1] Susan Hubbard,[1] Yoram Rubin,[2] Chris Murray,[3] Eric Roden,[4] and Ernest Majer[1]

Received 12 November 2003; revised 1 July 2004; accepted 6 October 2004; published 22 December 2004.

[1] The study demonstrates the use of ground-penetrating radar (GPR) tomographic data for estimating sediment geochemical parameters using data collected at the Department of Energy South Oyster bacterial transport site in Virginia. By exploiting the site-specific mutual dependence of GPR attenuation and extractable Fe(II) and Fe(III) concentrations on lithofacies, we develop a statistical model in which lithofacies and Fe(II) and Fe(III) concentrations at each pixel between the boreholes are considered as random variables. The unknown variables are estimated by conditioning to the colocated GPR data and the lithofacies measurements along boreholes using a Markov Chain Monte Carlo method. Cross-validation results show that the geophysical data, constrained by lithofacies, have the potential for providing high-resolution, multidimensional information on extractable Fe(II) and Fe(III) concentrations at the South Oyster site. *INDEX TERMS:* 1831 Hydrology: Groundwater quality; 1869 Hydrology: Stochastic processes; 3230 Mathematical Geophysics: Numerical solutions; 0689 Electromagnetics: Wave propagation (4275); 1099 Geochemistry: General or miscellaneous; *KEYWORDS:* geochemical characterization, geophysical data, MCMC, statistical model

Citation: Chen, J., S. Hubbard, Y. Rubin, C. Murray, E. Roden, and E. Majer (2004), Geochemical characterization using geophysical data and Markov Chain Monte Carlo methods: A case study at the South Oyster bacterial transport site in Virginia, *Water Resour. Res.*, *40*, W12412, doi:10.1029/2003WR002883.

1. Introduction

[2] Geochemical characterization is important for developing efficient bioremediation approaches for cleaning up metal and radionuclide contaminants in aquifers. Many studies have shown that both in situ physical and chemical heterogeneity control field-scale bacterial movement [*DeFlaun et al.*, 1997; *Chapelle*, 2001; *Mailloux et al.*, 2003]. For example, for those bacteria with low or neutral surface charges, the adhesion of bacteria to sediment is primarily determined by physical heterogeneity, specifically by grain size and pore throat size distributions [*Dong et al.*, 2002]. However, for those bacterial strains bearing high negative surface charges and traveling through the heterogeneous subsurface, chemical heterogeneity becomes important due to surface electrostatic interactions [*Scholl and Harvey*, 1992; *Mills et al.*, 1994; *Knapp et al.*, 2002].

[3] Traditional methods for characterizing geochemical heterogeneity typically involve drilling a borehole, and either retrieving a soil sample for laboratory analysis or collecting borehole logs within the hole. Although these methods are deemed necessary for collecting data to understand field-scale bacterial transport processes, it is prohibitive to use them intensively for collecting dense data to estimate geochemical parameters in a multidimensional domain. As a result, borehole sampling methods should be used together with cost effective and less invasive techniques, such as geophysical methods, for improved geochemical characterization.

[4] In our previous study, we have successfully estimated the high-resolution spatial distribution of hydraulic conductivity at the Department of Energy South Oyster bacterial transport site in Virginia using geophysical data [*Chen et al.*, 2001; *Hubbard et al.*, 2001]. Comparison of field tracer experiment measurements and numerical modeling predictions suggests that the estimated hydraulic conductivity values, obtained using geophysical tomographic approaches, provide information at a resolution that greatly improves the prediction of field-scale solute transport [*Scheibe and Chien*, 2003] and helps to improve the understanding of bacterial transport and attachment [*Mailloux et al.*, 2003].

[5] In this study, we explore the use of the same type of geophysical data sets for characterizing geochemical heterogeneity at the South Oyster bacterial transport site. We choose to estimate the spatial distribution of extractable Fe(II) and Fe(III) concentrations because many studies have shown that metal oxyhydroxide coatings (iron, aluminum, and manganese) have the potential to exert a strong influence on bacterial transport in aquifers [*Scholl and*

[1] Lawrence Berkeley National Laboratory, Berkeley, California, USA.
[2] Department of Civil and Environmental Engineering, University of California, Berkeley, California, USA.
[3] Pacific Northwest National Laboratory, Richmond, Washington, USA.
[4] Department of Biological Sciences, University of Alabama, Tuscaloosa, Alabama, USA.

0043-1397/04/2003WR002883$09.00

Harvey, 1992; *DeFlaun et al.*, 1997; *Fuller et al.*, 2000; *Knapp et al.*, 2002; *Mailloux et al.*, 2003]. At the South Oyster site, iron coatings have been recognized as one of the most important factors for understanding bacterial transport [*DeFlaun et al.*, 1997; *Dong et al.*, 2002; *Mailloux et al.*, 2003].

[6] Our goal in this study is to demonstrate the use of ground-penetrating radar (GPR) tomographic data for estimating solid phase Fe(II) and Fe(III) concentrations using a Markov Chain Monte Carlo (MCMC) method. We strive to provide high-resolution information on extractable Fe(II) and Fe(III) concentrations on a two-dimensional domain for other studies. Although we focus herein on the estimates of iron distribution, the methodology that we present can be used to estimate other geochemical parameters, given the availability of geophysical data and relationships that link the geophysical and geochemical attributes.

[7] The remainder of this paper is organized as follows. Section 2 describes site information and available data, and sections 3 and 4 describe the development of the statistical estimation method. Estimation results and cross validation of the method are given in section 5.

2. Site Information and Data

2.1. Site Information

[8] The South Oyster site is located on the southern Delmarva Peninsula, which is situated on the eastern coast of the United States between the Chesapeake Bay and Atlantic Ocean (Figure 1). The surficial unconfined aquifer underlying the study area consists of unlithified to weakly cemented, well-sorted, medium- to fine-grained sands and pebbly sands, and the water table is located ~2 m below the ground surface. A field-scale experiment within the uncontaminated aquifer at the site was undertaken by a multidisciplinary research team to evaluate the importance of chemical and physical heterogeneity in controlling bacteria transport at the site [*DeFlaun et al.*, 2001; *Johnson et al.*, 2001]. Two focus areas exist within the South Oyster site: the Narrow Channel Focus Area and the South Oyster Focus Area (SOFA). Forced gradient chemical and bacterial tracer test experiments were performed at both focus areas.

[9] This study focuses on data collected within a saturated aquifer at a site located ~15 m along geological strike from the SOFA transport site (Figure 1). Our goal is to investigate the spatial heterogeneity of geochemical parameters as an analogue to the immediately adjacent SOFA site. The available data include the laboratory measurements of physical, geological, and geochemical parameters from the cores retrieved from wells D1, D2, and D3. The samples were taken between depths of 2.4 m and 8.7 m below the ground surface with a sampling interval of 0.15 m to 0.30 m [*Johnson et al.*, 2001]. The data also include high-resolution ground-penetrating radar (GPR) and seismic tomograms acquired along the cross sections between wells D1-D2 and D2-D3 (Figure 1). We have performed multivariate data analysis for all the data sets and found lithofacies and GPR attenuation to be most informative for estimating extractable Fe(II) and Fe(III) concentrations. As such, in the following, we only describe the lithofacies, GPR attenuation, and solid phase Fe(II) and Fe(III) data, and explore their cross correlations.

2.2. Data Analysis

2.2.1. Lithofacies

[10] Borehole lithofacies categorization was performed for the study during the logging and core sampling process based on the visual grain size estimation using a comparator chart and on the soil color and texture description. In the original data, four lithofacies categories were identified: peat, mud, muddy sand, and sand. On the basis of cluster analysis of physical properties, we reduce the classifications from four to two categories, by grouping peat and mud together, and referring to it as mud, and by grouping muddy sand and sand together, and referring to it as sand.

[11] The spatial structure of lithofacies has been investigated using variograms, which are defined as the average squared difference of a quantity at two locations as a function of the measurement separation distance [*Rubin*, 2003]. We perform variogram analysis along the vertical direction by first computing the experimental variogram using the coded lithofacies data (sand = 1 and mud = 0) collected from wells D1, D2, and D3, and then fitting it using an exponential model with an integral scale of 0.5 m. Similarly, we attempt to fit a model to the experimental variogram in the horizontal direction, but with data from just three wells, no model could be reliably fit to the horizontal variogram due to sparse sample density in that direction. In this study, however, we assume an anisotropy ratio of 5, borrowed from the nearby Narrow Channel Focus Area [*Hubbard et al.*, 2001], and use an integral scale of 2.5 m in the horizontal direction.

2.2.2. GPR Attenuation

[12] GPR is a geophysical tool that has become increasingly popular as researchers across a variety of disciplines strive to better understand near-surface conditions. GPR uses electromagnetic energy at frequencies of 50–1500 MHz to probe the subsurface. At the frequencies used and under the low-loss conditions, the electromagnetic signals propagate primarily as waves, and the GPR attributes are functions of dielectric constant and electrical conductivity of the medium [*Davis and Annan*, 1989]. Radar velocities are influenced by the dielectric constant, which is sensitive to water content and porosity, and thus have been used for mapping soil water content in unsaturated systems [*Hubbard et al.*, 1997; *Binley and Beven*, 2003] and hydraulic conductivity in saturated systems [*Chen et al.*, 2001; *Hubbard et al.*, 2001]. Radar amplitudes (or attenuation), however, are influenced by both the dielectric constant and the electric conductivity of the medium [*Davis and Annan*, 1989]. In saturated aquifers, such as the one considered here, radar attenuation usually is dominated by electrical conductivity, and high electrical conductivity often leads to high radar attenuation. Since fine-grained soils (such as clay and silt) typically have much higher electrical conductivity (2–1000 mS/m for clay and 1–100 mS/m for silt) than that of coarse-grained soils such as sand (0.1–1 mS/m), higher radar attenuation is often associated with high clay content and silt fraction. Although the salinity of pore fluid may also influence GPR attenuation, it does not appear to be a factor at this site because the overall salinity of the pore fluid is very low (less than 0.03 wt%). Consequently, we

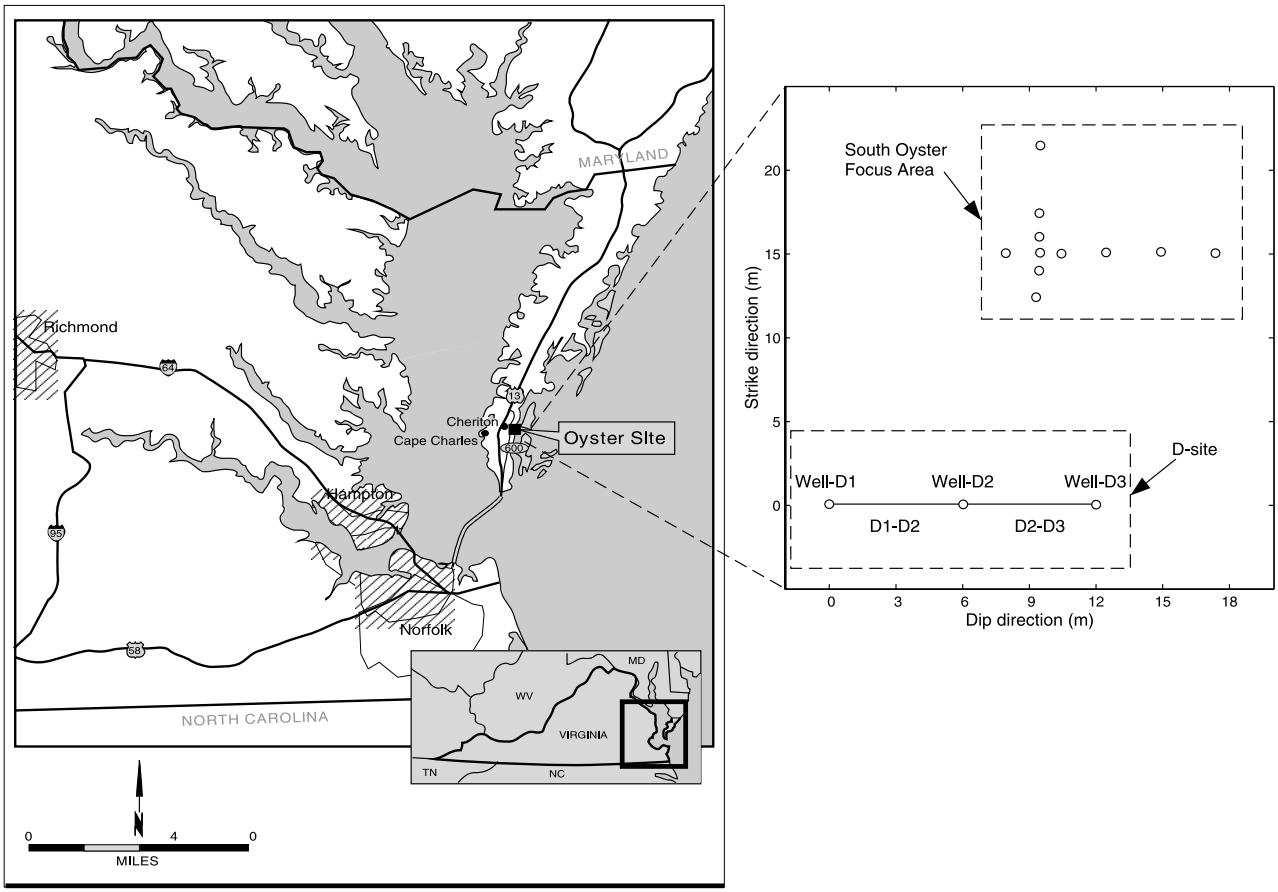

Figure 1. Locations of the South Oyster bacterial transport site and our study area (D-site). Well bore data were collected at wells D1, D2, and D3, and ground-penetrating radar (GPR) attenuation tomograms were collected along transects D1-D2 and D2-D3.

hypothesize that both GPR attenuation and geochemical parameters are predominantly influenced by lithology, and focus herein on the use of GPR attenuation to estimate geochemical parameters by exploring the lithology link.

[13] GPR tomographic data were collected along the cross sections between wells D1 and D2 and between wells D2 and D3, using borehole antennas having a central frequency of 100 MHz. A typical cross-hole tomographic geometry consists of two vertical boreholes separated by an interwell region of interest. Direct energy from a transmitting antenna in one borehole is recorded by the receiving antenna located in the other borehole. By moving the transmitting and receiving antennas in the boreholes, many ray paths can be recorded, which can be inverted to provide a tomographic image of the region between the boreholes [*Peterson et al.*, 1985]. The recorded data include the direct electromagnetic wave travel time from the transmitter to the receiver passing through the cross-hole region and the amplitude of the direct arrivals. After dividing the interwell area into a grid of pixels (0.25 m $\times$ 0.25 m), an inversion algorithm was used to transform the recorded travel time and amplitude information into estimates of the GPR velocity and attenuation at each pixel following *Peterson* [2001]. Figure 2a shows a contoured GPR attenuation tomogram along the cross section between wells D1 and D3. GPR attenuation data "overlap" with borehole data at or near the borehole locations. These colocated data are used to develop site-specific relations between geophysical attributes and geochemical parameters. The developed relationships are then used in conjunction with the GPR tomographic data (Figure 2a) to extrapolate borehole geochemical measurements into the interwell areas.

[14] Figure 3 shows the relationship between the sand and mud lithofacies and the natural logarithmic GPR attenuation. As expected from the previous discussions, the GPR amplitudes are more attenuated when passing through mud than through sand. On the basis of data collected at the three wells, the mean logarithmic GPR attenuation of sand is -0.74 1/m with a standard deviation of 0.23 1/m, while the mean logarithmic GPR attenuation of mud is -0.33 1/m with a standard deviation of 0.36 1/m.

2.2.3. Extractable Fe(II)

[15] Extractable Fe(II) concentrations were measured by leaching triplicate 0.5–1.0 g subsamples, obtained from each depth interval of wells D1, D2, and D3, with 0.5 M HCl for one hour. The Fe(II) versus Fe(III) content of the extracts was determined using Ferrozine [*Roden and Lovely*, 1993]. The exact nature of the Fe(II)-bearing phases leached by the 0.5 M HCl is unknown, but may generally include Fe(II) from native iron-bearing minerals in the formation (e.g., carbonates or silicates), as well as Fe(II) phases produced from bacterial Fe(III) oxide reduction (e.g., siderite or Fe(II) sorbed to residual Fe(III) oxides or other mineral surfaces).

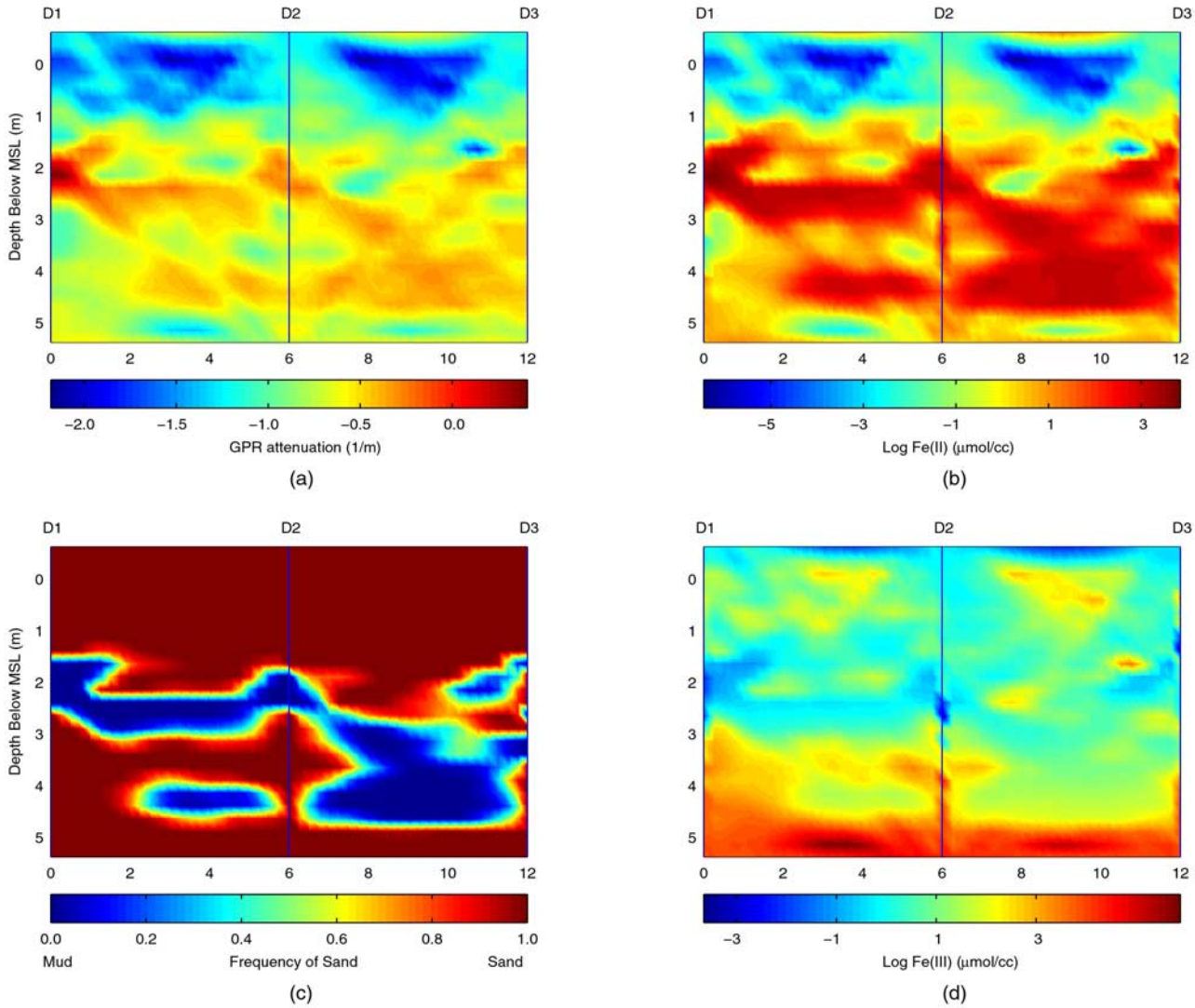

Figure 2. (a) GPR attenuation. (b) Estimated mean natural logarithmic Fe(II) concentrations. (c) Frequency of sand (a frequency of 0.0 implies that lithofacies is mud, whereas a frequency of 1.0 implies that lithofacies is sand). (d) Estimated mean natural logarithmic Fe(III) concentrations. At wells D1, D2, and D3 of Figures 2b–2d the measured values rather than the estimated values of Fe(II), frequency of sand, and Fe(III) are used.

[16] Figure 4 shows the histograms of the natural logarithmic extractable Fe(II) concentrations for sand and mud based on data collected at wells D1, D2, and D3. The figure suggests that the distributions of logarithmic Fe(II) concentrations are symmetrical around the corresponding means for both sand and mud. However, the logarithmic Fe(II) concentrations of sand have a much larger range (from −4 to 4) than those of mud (from 2 to 4). The logarithmic Fe(II) concentrations also depend on lithofacies; mud has much higher extractable Fe(II) concentrations compared to sand. The mean natural logarithmic Fe(II) concentration of mud is 3.12 μmol/cc with a standard deviation of 0.58 μmol/cc, whereas the mean natural logarithmic Fe(II) concentration of sand is only 0.25 μmol/cc with a standard deviation of 1.66 μmol/cc. The logarithmic Fe(II) concentration distributions as a function of lithofacies are reasonable, as Fe(II) is usually sequestered in fine-grain sediments such as silt and clay [*Chapelle*, 2001], and our mud lithofacies include both silt and clay components.

[17] As both logarithmic Fe(II) concentrations and logarithmic GPR attenuation display a correlation with lithofacies, we have physical justification for investigating the link between Fe(II) concentrations and GPR attenuation. The connection, however, may be affected by organic matter, grain size, porosity, and other physical parameters. Figure 5 shows a cross plot of logarithmic Fe(II) concentrations versus logarithmic GPR attenuation based on data at wells D1, D2, and D3, where the circles represent sand and the triangles represent mud. This figure reveals that for both sand and mud, logarithmic Fe(II) concentrations linearly increase with increasing logarithmic GPR attenuation. For mud, however, the increase is not as apparent as for sand.

2.2.4. Extractable Fe(III)

[18] The concentrations of extractable Fe(III), including amorphous and crystalline Fe(III) oxides, were determined

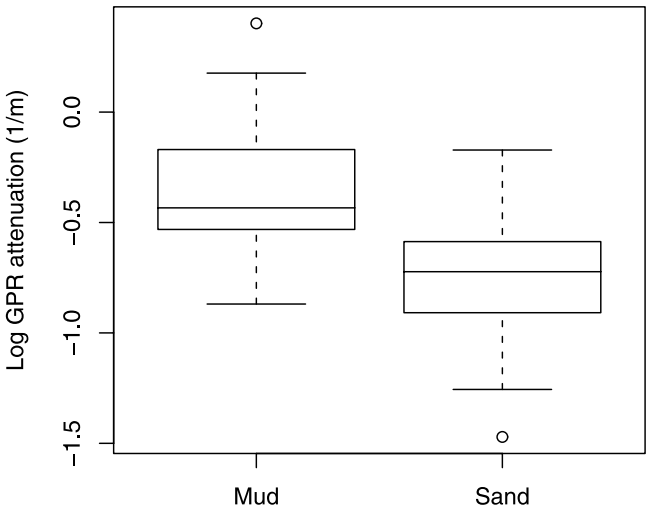

Figure 3. Box plot of natural logarithmic GPR attenuation.

using a citrate-dithionite (CD) reagent (pH 4.8) [*Canfield*, 1989]. The 0.5 M HCl extractable Fe(II) content of parallel sediment extracts (see above) was subtracted from total CD extractable Fe in order to estimate Fe(III) abundance, as the CD reagent typically recovers the majority of solid phase Fe(II) compounds. The total Fe generally increases with depth in the sediment as illustrated by *Wildung et al.* [2004]. However, no detailed information is available about the depositional or postdepositional processes responsible for the observed Fe distribution.

[19] Figure 6 shows the histograms of natural logarithmic Fe(III) concentrations for sand and mud. The logarithmic Fe(III) concentrations of mud are symmetric around its mean and the logarithmic Fe(III) concentrations of sand are slightly skewed toward the larger values. Although the mean values of the logarithmic Fe(III) concentrations for sand (2.12 μmol/cc) and for mud (−0.60 μmol/cc) are quite different, their ranges overlap considerably. In addition, the logarithmic Fe(III) concentrations have weak linear correlations with both logarithmic GPR attenuation (R^2 = 0.05) and logarithmic Fe(II) concentrations (R^2 = 0.15), but have a relatively good correlation with depth (R^2 = 0.37).

3. Statistical Model

[20] This section describes the statistical model for estimating the spatial distribution of Fe(II) and Fe(III) concentrations along the cross section between wells D1 and D3. Within the statistical framework, unknown Fe(II) and Fe(III) concentrations and lithofacies at each location between the wells are considered as random variables, which are fully characterized by the joint conditional probability function given GPR tomographic data and borehole lithofacies logs. Estimation of those variables from the joint probability function is obtained using a Markov Chain Monte Carlo approach, which will be described in the next section.

3.1. Model Setup

[21] The developed statistical model is intended to meet conditions that are specific to our study site, although its underlying concept is quite general and can be applied to other sites. Figure 7 shows a discretization of the cross section (12 m × 6 m) between wells D1 and D3. There are a total number of 1225 pixels, each of which has dimensions of 0.25 m × 0.25 m. Lithofacies and Fe(II) and Fe(III) concentrations are known at pixels along wells D1, D2, and D3, but are unknown at pixels located between the wells. GPR attenuation is considered to be known at all locations along the two-dimensional transect. Our goal is to estimate all the unknown parameters given data available at the three wells and along the cross section.

[22] The estimation problem can be addressed in a stochastic framework using a joint conditional probability function. Let L_i be the indicator random variable representing lithofacies at pixel i, 1 for sand and 0 for mud, $i \in N$, where N is the index set of all pixels where lithofacies and Fe(II) and Fe(III) concentrations are unknown. Let X_i and Y_i denote the unknown logarithmic Fe(II) and Fe(III) concentrations at pixel i. For convenience, we shall refer to

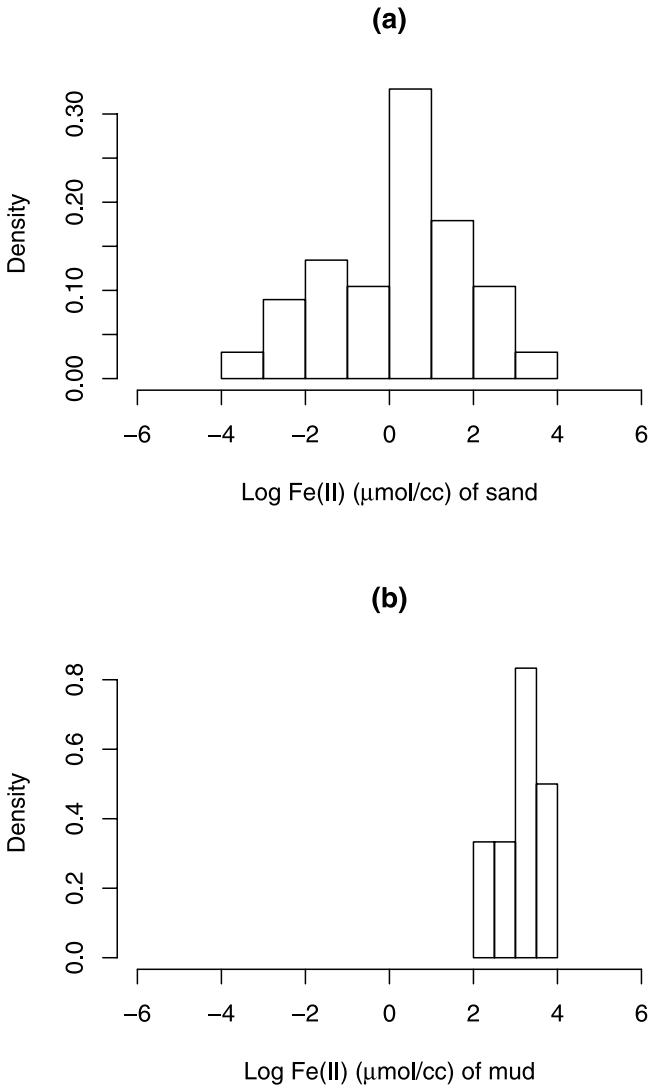

Figure 4. Histograms of natural logarithmic Fe(II) concentrations of (a) sand and (b) mud as a function of lithofacies.

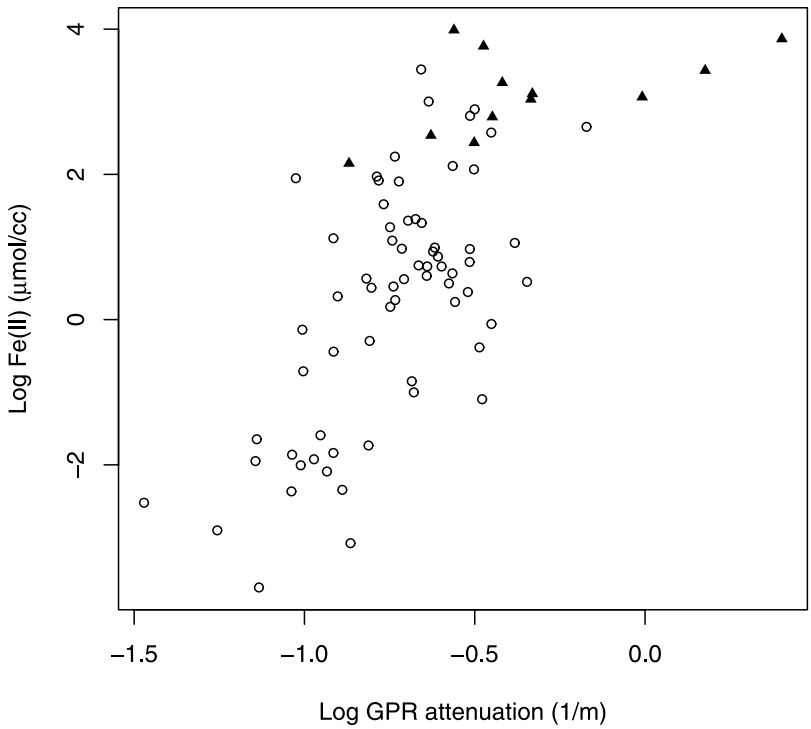

Figure 5. Cross plot of natural logarithmic Fe(II) concentrations versus natural logarithmic GPR attenuation, where the circles represent sand samples and the solid triangles represent mud samples.

probability functions and probability density functions as probability distributions in the later text. Let a_i denote the inverted logarithmic GPR attenuation at pixel i and l_w denote the known lithofacies at the borehole pixels. Following the convention suggested by *Gelfand and Smith* [1990], we use square brackets to denote probability distributions. Consequently, the joint conditional distribution is given by

$$[\{L_i\}, \{X_i\}, \{Y_i\}|\{a_i\}, \{l_w\}], \qquad i \in N \tag{1}$$

where { } denotes a set that includes all possible values of the variable. Our objective is to obtain the marginal distribution functions of lithofacies and logarithmic Fe(II) and Fe(III) concentrations at each pixel from the joint conditional distribution.

3.2. Local Conditional Distribution

[23] We can simplify equation (1) by considering local dependence between logarithmic GPR attenuation, lithofacies, and logarithmic Fe(II) and Fe(III) concentrations, using data collected at boreholes. We use the stepwise deletion technique [*Chen et al.*, 2001] to obtain the best regression models for logarithmic Fe(II) and Fe(III) concentration estimation. We also fit the logarithmic GPR attenuation as a linear function of the lithofacies indicator. Figure 8 is a graphical model showing the local conditional relationships among lithofacies, logarithmic GPR attenuation, and logarithmic Fe(II) and Fe(III) concentrations. We found that logarithmic Fe(II) concentrations depend on the colocated lithofacies and logarithmic GPR attenuation, and logarithmic Fe(III) concentrations depend on the colocated logarithmic Fe(II) concentrations and depth. On the basis of data analysis, we assume each of the local conditional distribution to be Gaussian as follows:

$$[a_i|L_i] \sim \text{Normal}(u_1 + u_2 L_i, \tau_1), \tag{2}$$

$$[X_i|a_i, L_i] \sim \text{Normal}(v_1 + v_2 L_i + v_3 a_i + v_4 L_i a_i, \tau_2), \tag{3}$$

$$[Y_i|X_i] \sim \text{Normal}(r_1 + r_2 X_i + r_3 d_i, \tau_3), \tag{4}$$

where d_i is depth at pixel i, u_1, u_2, v_1, v_2, v_3, v_4, r_1, r_2, and r_3 are regression coefficients, and τ_1, τ_2, and τ_3 are the inverse variances of the conditional distributions of a_i, X_i, and Y_i, respectively. The coefficients and inverse variances, obtained from data analysis, are given in Table 1. The goodness of each regression model can be evaluated using the multiple correlation coefficients given in the table.

[24] In equations (3) and (4), we assume that logarithmic Fe(II) and Fe(III) concentrations are spatially independent given the other colocated parameters. The spatial continuity of Fe(II) and Fe(III) concentrations are preserved to some point through their links to lithofacies and GPR attenuation. This assumption may lead to slight discontinuity of logarithmic Fe(II) and Fe(III) concentration estimation around boreholes. To consider logarithmic Fe(II) and Fe(III) concentrations as spatial variables, however, we need to develop reliable cross variograms, which is not possible using data at only three boreholes.

3.3. Joint Conditional Distribution

[25] We can expand equation (1) into several terms using Bayes's theorem [*Bernardo and Smith*, 1994]. On the basis

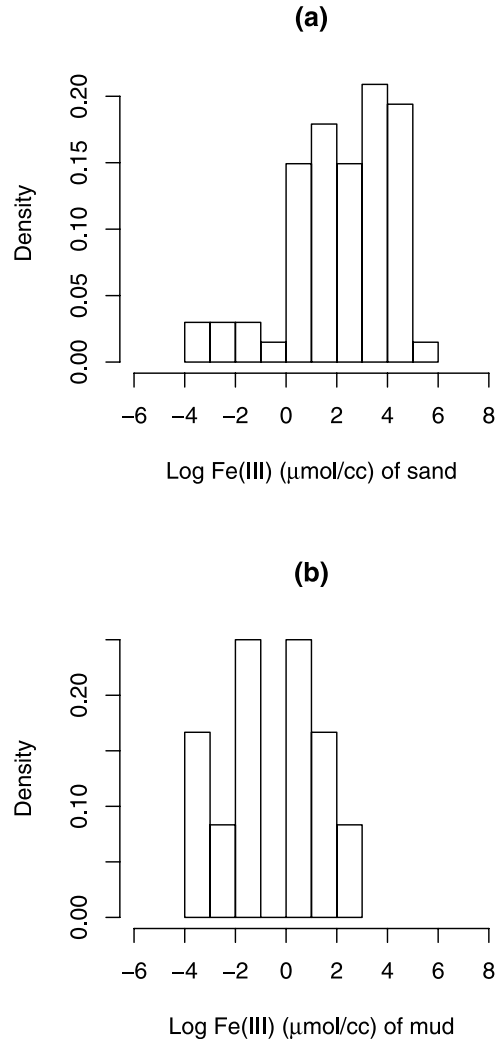

Figure 6. Histograms of natural logarithmic Fe(III) concentrations of (a) sand and (b) mud.

of the dependence relationships shown in Figure 8, the equation can be expanded as follows:

$$[\{L_i\},\{X_i\},\{Y_i\}|\{a_i\},\{l_w\}] \propto [\{Y_i\}|\{X_i\}][\{X_i\}|\{a_i\},\{L_i\}] \quad [\{a_i\}|\{L_i\}][\{L_i\},\{l_w\}], \tag{5}$$

where "$\propto$" represents "proportional to," which ignores the normalizing constant at the right side of equation (5). By assuming that the values of logarithmic GPR attenuation and logarithmic Fe(II) and Fe(III) concentrations at each pixel are conditionally independent of the ones at other pixels, we obtain the following form of the joint distribution:

$$[\{L_i\},\{X_i\},\{Y_i\}|\{a_i\},\{l_w\}] \propto [\{L_i\},\{l_w\}] \prod_{i\in N}\{[Y_i|X_i][X_i|a_i,L_i][a_i|L_i]\}. \tag{6}$$

Equation (6) can be determined by incorporating the local conditional distributions given in equations (2)–(4).

4. MCMC Sampling Method

[26] This section outlines the method for obtaining estimates of Fe(II) and Fe(III) concentrations from the joint conditional distribution shown in equation (6). As conventional analytical approaches are not feasible due to the large number of unknown variables involved, we instead use a Markov Chain Monte Carlo method, which has recently emerged as a powerful approach for solving complex statistical problems that involve a large number of dependent random variables. The MCMC method provides an efficient way to draw samples of unknown variables from their joint distributions by running a constructed Markov chain [*Gilks et al.*, 1996]. Using those samples, we can obtain the mean, variance, predictive intervals, and even probability function for each variable. Several applications of MCMC methods to hydrology have been found, including those documented by *Bosch* [1999], *Bates and Campbell* [2001], and *Michalak and Kitanidis* [2003].

[27] We estimate Fe(II) and Fe(III) concentrations by following four basic steps: (1) derive the conditional distribution for each unknown variable given all the data and all

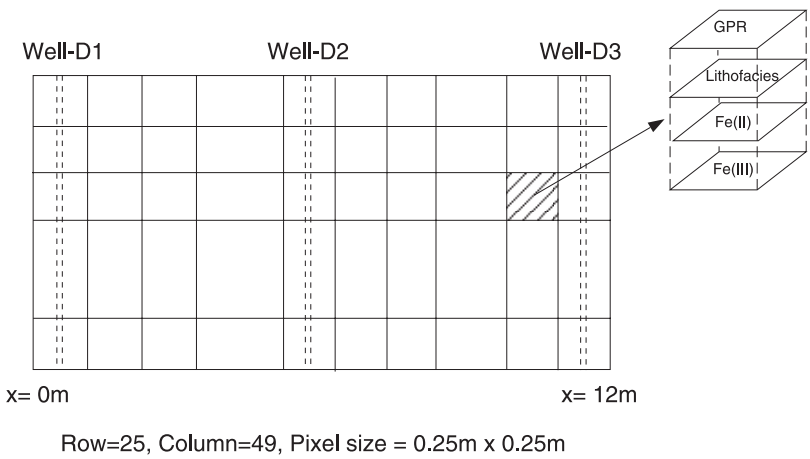

Figure 7. Discretization of the cross section between wells D1 and D3. The total number of pixels is $25 \times 49 = 1225$.

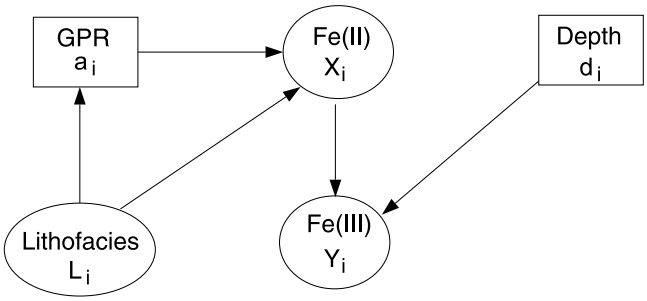

Figure 8. Graphical model showing the local dependence relationships among lithofacies, GPR attenuation, depth, and Fe(II) and Fe(III) concentrations. The rectangles represent given data, and the ellipses represent unknown variables.

other variables, which is referred to as the full conditional distribution of the variable; (2) sequentially draw samples from each of the conditional distributions; (3) monitor convergence using the method developed by *Gelman and Rubin* [1992]; (4) make inferences about each variable using the generated samples. The first three steps of the process are described below, and the final stage is given in section 5.

4.1. Deriving Full Conditional Distributions

[28] Full conditional distributions play a prominent role in applications of MCMC methods [*Gilks et al.*, 1996]. They are typically not the same as the local conditional distributions that are conditioned to all the data but only subsets of all other variables. However, we can derive full conditional distributions by using the local conditional distributions. Theoretically, the full conditional distribution of each variable is proportional to the joint conditional distribution shown in equation (6). As MCMC methods need no information about normalizing constants, we can obtain the full conditional distribution of each variable by omitting the terms at the right side of equation (6) that are not directly related to the variable.

4.1.1. Full Conditional Probability Density Function of Y_i

[29] Let $[Y_i|\cdot]$ denote the full conditional probability density function (pdf) of Y_i given all the data and other variables. After omitting all the terms in equation (6) that are not directly related to Y_i, we can obtain

$$[Y_i|\cdot] \propto [Y_i|X_i]. \tag{7}$$

This is the same as the local conditional pdf of Y_i given X_i that was shown in equation (4).

4.1.2. Full Conditional Probability Density Function of X_i

[30] Similarly, by omitting all the terms in equation (6) that are not directly related to X_i, we can obtain the full conditional pdf of X_i as follows:

$$[X_i|\cdot] \propto [Y_i|X_i][X_i|a_i, L_i]. \tag{8}$$

By substituting $[X_i|a_i, L_i]$ and $[Y_i|X_i]$ with equations (3) and (4), respectively, and after some derivations (Appendix A), we can obtain

$$[X_i|\cdot] \sim Normal \cdot \left(\frac{\tau_2(v_1 + v_2L_i + v_3a_i + v_4L_ia_i) + r_2\tau_3(Y_i - r_1 - r_3d_i)}{\tau_2 + r_2^2\tau_3}, \tau_2 + r_2^2\tau_3\right). \tag{9}$$

4.1.3. Full Conditional Probability Function of L_i

[31] The MCMC method allows us to consider lithofacies as a spatially correlated random variable. As a result, we can incorporate spatial correlation and borehole lithofacies measurements into the estimation model. Similar to the derivations of $[Y_i|\cdot]$ and $[X_i|\cdot]$, we omit those terms in equation (6) that are not directly related to L_i and obtain

$$[L_i|\cdot] \propto [a_i|L_i][X_i|a_i, L_i]\left[L_i|\{L_j, j \neq i\}, \{l_w\}\right], \tag{10}$$

where $\{L_j, j \neq i\}$ is the set including lithofacies at all pixels except pixel i. It is convenient and reasonable to assume that lithofacies L_i depends only on the lithofacies at its adjacent pixels [*Chen and Rubin*, 2003]. Let set A_i be the index set of the adjacent pixels of pixel i. For those pixels not near boreholes, the conditional probability of L_i does not depend on borehole lithofacies measurements, and thus it is given by

$$\left[L_i|\{L_j, j \neq i\}, \{l_w\}\right] = \left[L_i|L_j, j \in A_i\right] \sim \text{Bernoulli}(p_i^*), \tag{11}$$

where p_i^* is the probability of lithofacies being sand given the lithofacies at its surrounding pixels, which is obtained using indicator kriging [*Rubin*, 2003] (Appendix B). Although for those pixels near boreholes, the conditional probability of L_i also depends on the borehole lithofacies measurements $\{l_w\}$, we can use a similar method as described in Appendix B to obtain probability p_i^*.

[32] By substituting $[a_i|L_i]$ and $[X_i|a_i, L_i]$ with equations (2) and (3), respectively, and after some simplifica-

Table 1. Coefficients of Cross Correlations Among Lithofacies, Geochemical Parameters, and Geophysical Data Corresponding to Equations (2)–(4)

Models	Coefficients
Logarithmic GPR attenuation	$u_1 = -0.3332$, $u_2 = -0.4110$, $\tau_1 = 15.58$
Versus lithofacies	$R^2 = 0.26$
Logarithmic Fe(II) concentration	$v_1 = 3.4128$, $v_2 = 0.3085$, $v_3 = 0.8796$
Versus lithofacies and logarithmic GPR attenuation	$v_4 = 3.7870$, $\tau_2 = 0.70$, $R^2 = 0.60$
Logarithmic Fe(III) concentration	$r_1 = -0.8813$, $r_2 = -0.5910$, $r_3 = 1.0026$
Versus depth and logarithmic Fe(II) concentration	$\tau_3 = 0.45$, $R^2 = 0.60$

tions (Appendix C), we can obtain the full conditional probability of lithofacies as follows:

$$[L_i|\cdot] \sim \text{Bernoulli}\left(\frac{p_i^* p_i}{1 - p_i^* + p_i^* p_i}\right), \tag{12}$$

where

$$p_i = \exp\{\tau_1 u_2 (a_i - u_1 - 0.5u_2) + \tau_2 (v_2 + v_4 a_i) \\ (X_i - v_1 - 0.5v_2 - v_3 a_i - 0.5v_4 a_i)\}.$$

4.2. Sampling Full Conditional Distributions

[33] The relationships shown in equations (7), (9), and (12) represent the full conditional distributions of all variables of interest. The second step of the MCMC method is to sequentially draw samples from those distributions. There are two major algorithms that can be used to draw samples from full conditional distributions: the Gibbs sampler [*Geman and Geman*, 1984] and the Metropolis-Hastings method [*Metropolis et al.*, 1953; *Hastings*, 1970]. As the full conditional distributions of X_i and Y_i are Gaussian and the full conditional distribution of L_i is Bernoulli, which are easily sampled, we use in this study the Gibbs sampler. The main steps are as follows: (1) for each $i \in N$, randomly assign 0 or 1 to L_i and refer to it as $L_i^{(0)}$, assign a real number to X_i and refer to it as $X_i^{(0)}$, and assign a real number to Y_i and refer to it as $Y_i^{(0)}$. Let $k = 1$. (2) For each randomly selected $i \in N$, draw a sample from the Gaussian distribution $[Y_i|\cdot]$ (equation (4)) given $X_i^{(k-1)}$ and refer to it as $Y_i^{(k)}$. (3) For each randomly selected $i \in N$, draw a sample from the Gaussian distribution $[X_i|\cdot]$ (equation (9)) given $Y_i^{(k)}$ and $L_i^{(k-1)}$, and refer to it as $X_i^{(k)}$. (4) For each $i \in N$, draw a sample from the Bernoulli distribution $[L_i|\cdot]$ (equation (12)) given $X_i^{(k)}$, $\{L_j^{(k)}, j = 1, 2, \cdots, i - 1\}$, and $\{L_j^{(k-1)}, j = i + 1, \cdots, n\}$ and refer to it as $L_i^{(k)}$. (5) Let $k = k + 1$. If $k > m$, where m is the maximum number of iterations allowed, stop; otherwise, go to step 2.

4.3. Monitoring Convergence of the Sampling

[34] In the third step of the MCMC method, our goal is to determine the number of iterations that we need to obtain samples for inferences using the Gibbs sampler. Samples obtained from the preceding algorithm may not be the samples of their marginal conditional distributions. However, theoretically, after a sufficiently long run (for example t iterations), referred to as burn-in [*Gilks et al.*, 1996], samples $\{X_i^{(k)}, Y_i^{(k)}, L_i^{(k)}: k = t + 1, \cdots, m, i \in N\}$ obtained from the algorithm are approximately samples from their corresponding true marginal conditional distributions [*Gelfand and Smith*, 1990]. In addition, as indicated by the ergodic theorem [*Gilks et al.*, 1996], the mean of any measurable function of those variables obtained using the generated samples after discarding burn-in samples asymptotically converges to its true expectation as $m \to +\infty$.

[35] There are many methods for monitoring convergence and finding the burn-in, such as *Gelman and Rubin* [1992], *Geweke* [1992], and *Raftery and Lewis* [1992] methods. The most often used method is the *Gelman and Rubin* [1992] method. The method first entails running several Markov chains with very different initial values, followed by calculation of a criterion, referred to as the scale reduction score based on the multiple Markov chains [*Gelman and Rubin*, 1992]. If the scale reduction score is less than 1.2, the Markov chain is considered to be converged; otherwise, more runs are needed. Using the preceding convergence diagnostics method, we found that a burn-in of 400 realizations is enough for all the unknown variables in this study. After the burn-in stage, we continue to run the chain for another 2000 runs, and use all those samples to make inferences about the unknown variables. The total computing time for running the 2400 iterations is less than ten minutes on a Pentium-III personal computer.

5. Results and Discussion

[36] At the final stage of the MCMC method, we summarize the results of Fe(II) and Fe(III) concentration estimation. We first present the two-dimensional images of the mean logarithmic Fe(II) and Fe(III) concentrations, obtained using the previous MCMC method. We then show the results of cross-validation analysis that demonstrate the effectiveness of the developed statistical model. Finally, we provide a short discussion of our methodology.

5.1. Fe(II) and Fe(III) Estimation

[37] We have estimated the probability density functions of extractable Fe(II) and Fe(III) concentrations along the cross section between wells D1 and D3 using the method developed in sections 3 and 4, based on the lithofacies and Fe(II) and Fe(III) concentration data at wells D1, D2, and D3 and the GPR attenuation data along the cross sections from wells D1 to D3. Figure 2b shows the estimated mean logarithmic Fe(II) concentrations along the two-dimensional transect. The figure provides detailed spatial information about extractable Fe(II) concentrations on the cross section, which could not be obtained from borehole measurements only. The estimated spatial patterns of Fe(II) concentrations are similar to those of GPR attenuation (Figure 2a) because of the good correspondence of Fe(II) concentrations with GPR attenuation as shown in Figure 5. Figure 2d shows the two-dimensional image of logarithmic Fe(III) concentrations, which is much different from the GPR attenuation image. Comparison of Figures 2c and 2d reveals that extractable Fe(III) concentrations are higher beneath the mud layer than above the layer.

[38] As the byproduct of the Fe(II) and Fe(III) concentration estimation, we have also obtained the probability of sand occurring at each pixel on the cross section between wells D1 and D3 (Figure 2c). Lithofacies on the cross sections between wells D1 and D3 correspond to GPR attenuation very well, with sand having lower attenuation and mud having higher attenuation. Figure 2c also suggests that there is a mud layer in the middle of the cross section, which passes through the three wells.

[39] Slight discontinuity of estimated logarithmic Fe(II) and Fe(III) are observed around three well bores in Figures 2b and 2d. This is caused by our assumptions about the statistical model that Fe(II) and Fe(III) concentrations are spatially independent given the colocated GPR and lithofacies data. The model can be improved using a more complex method, such as the one used by *Bosch et al.* [2001] in

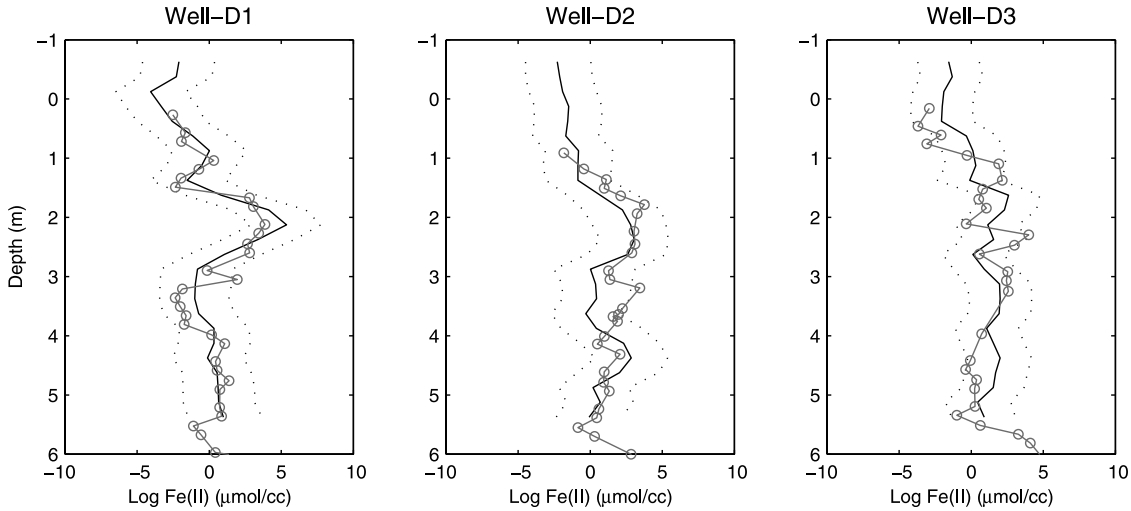

Figure 9. Comparisons of the true logarithmic Fe(II) concentrations and their corresponding estimated values obtained using GPR attenuation during the cross-validation exercise. The circles with solid lines represent the core measurements, the solid lines represent the mean estimates, and the dashed lines represent the 95% predictive intervals.

estimation of lithological structure from geophysical gravity and magnetic data.

5.2. Cross Validation

[40] Cross validation has been performed based on data at wells D1, D2, and D3 to assess the accuracy of our estimation method. We consider each well in turn as a testing well and the other two wells as training wells. As was previously performed using the entire data set, in this exercise, we first derive cross correlations among various types of properties and spatial correlation of lithofacies from only the training data set. We then estimate logarithmic Fe(II) and Fe(III) concentrations at the testing locations using data at the training wells and GPR attenuation data along the transect from wells D1 to D3. By comparing the estimated results with their corresponding true values at the testing well, we evaluate the effectiveness of the developed model for Fe(II) and Fe(III) concentration estimation.

[41] Figure 9 compares the estimated mean logarithmic Fe(II) concentrations (solid lines), obtained during this cross-validation exercise, with their corresponding core measurements (circles with solid lines) at testing wells D1, D2, and D3, respectively. The dashed lines indicate the 95% predictive intervals. The figure suggests that the developed model is effective for logarithmic Fe(II) concentration estimation. As shown in the figure, the mean estimates of logarithmic Fe(II) concentrations at well D1

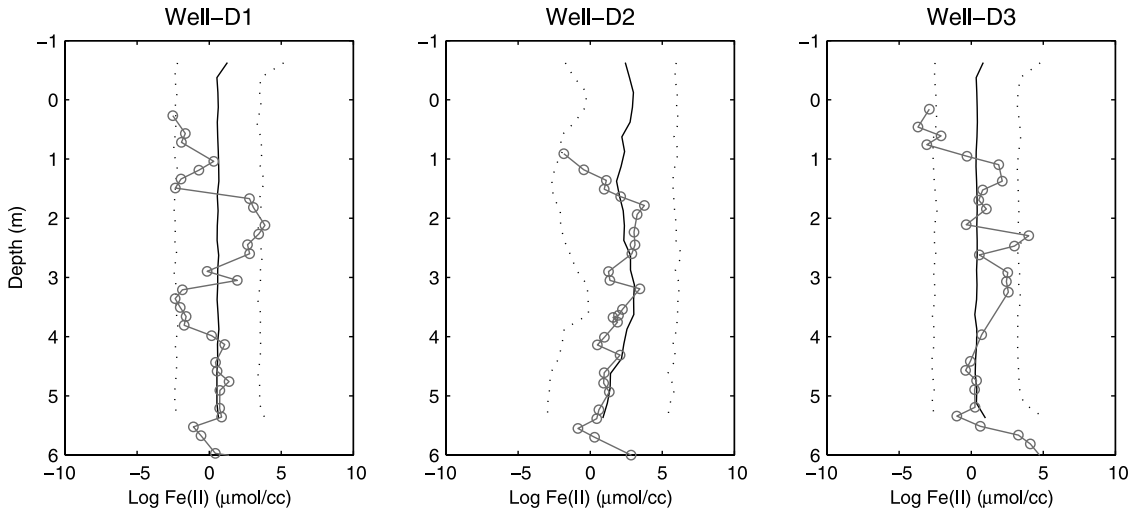

Figure 10. Comparisons of the true logarithmic Fe(II) concentrations and their corresponding estimated values obtained without using GPR attenuation during the cross-validation exercise. The circles with solid lines represent the core measurements, the solid lines represent the mean estimates, and the dashed lines represent the 95% predictive intervals.

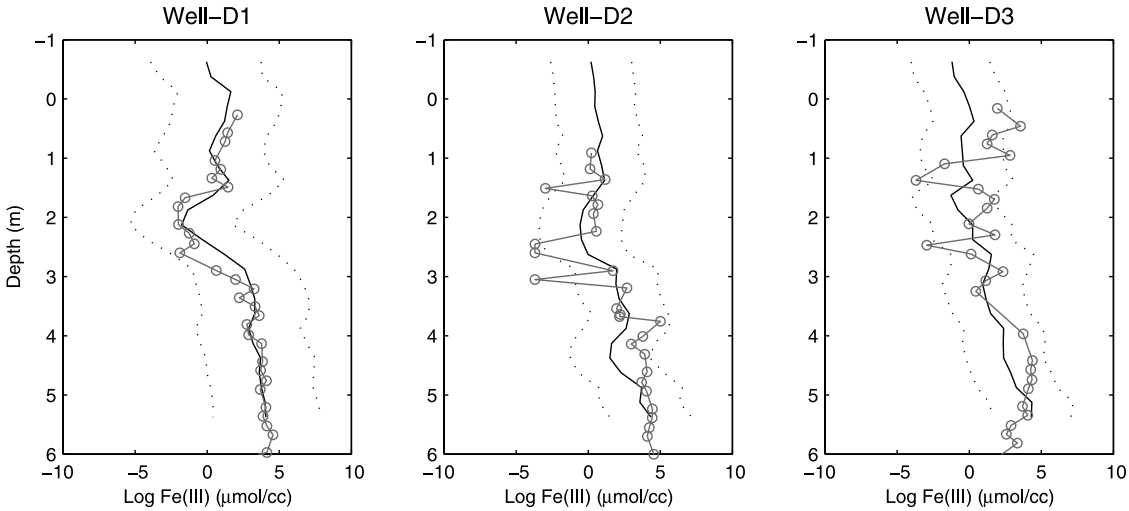

Figure 11. Comparisons of the true logarithmic Fe(III) concentrations and their corresponding estimated values obtained using GPR attenuation during the cross-validation exercise. The circles with solid lines represent the core measurements, the solid lines represent the mean estimates, and the dashed lines represent the 95% predictive intervals.

closely follow the true measurements of logarithmic Fe(II) concentrations, and the mean estimates of logarithmic Fe(II) concentrations at testing well D2 has a good agreement with the true values. Although the estimated results of logarithmic Fe(II) concentrations at testing well D3 are not as good as at other testing wells, most measurements are still within the 95% predictive intervals of the estimated values.

[42] Figure 10 shows the estimated mean logarithmic Fe(II) concentrations obtained without using GPR attenuation data in order to show the improvement offered by the GPR data. In this case, again, the solid lines represent the estimated values and the circles with solid lines represent the true values at the testing wells. Although the three wells in the cross section are separated by only 6 m, the estimated results without using GPR attenuation are much worse than those obtained with the use of GPR attenuation. This is especially apparent at testing well D1. The mean estimates of Fe(II) concentrations are smooth, and the 95% predictive intervals are larger than those of the model including GPR attenuation.

[43] Figure 11 shows the estimated mean logarithmic Fe(III) concentrations and their 95% predictive intervals at each testing well obtained during the cross validation. Again, Fe(III) concentration estimates at each testing well are obtained using only data at the other two training wells, along with the GPR attenuation, and a comparison of the estimates with the true data is given to assess the validity of our developed model. We found that the measured logarithmic Fe(III) concentrations follow the trends of the estimated

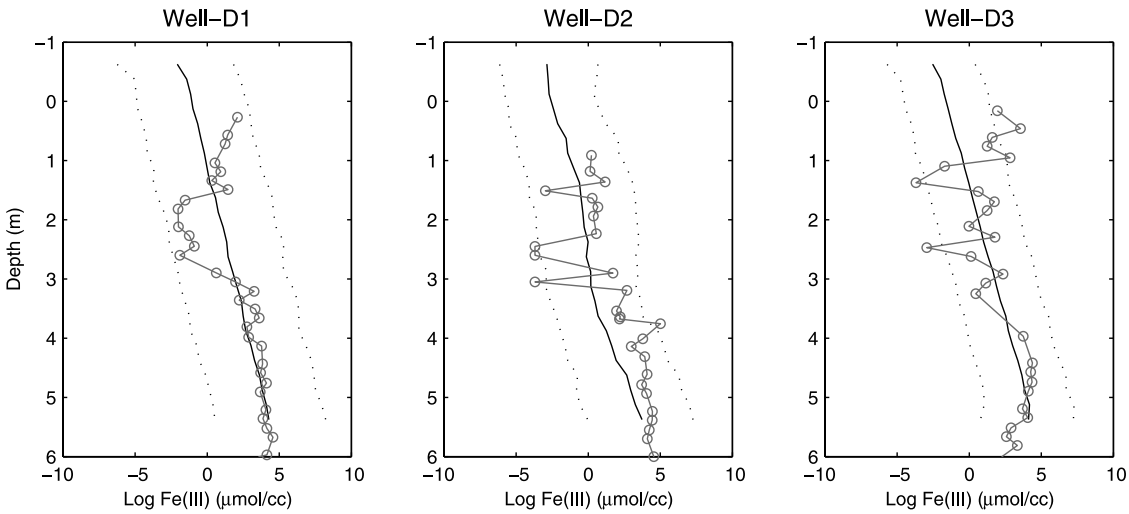

Figure 12. Comparisons of the true logarithmic Fe(III) concentrations and their corresponding estimated values obtained without using GPR attenuation during the cross-validation exercise. The circles with solid lines represent the core measurements, the solid lines represent the mean estimates, and the dashed lines represent the 95% predictive intervals.

mean, and that most of the estimates are within the 95% predictive intervals. Similar to Figure 10, Figure 12 shows the estimated mean logarithmic Fe(III) concentrations obtained without using GPR attenuation data. It is clear that GPR attenuation provides information for improving estimation of Fe(III) concentrations, especially for testing well D1.

5.3. Discussion

[44] We have demonstrated the use of geophysical tomographic data for estimating geochemical heterogeneity based on a field data set using a statistical model. The integration of cross-hole geophysical data and borehole measurements has the potential for providing high-resolution information about the spatial distribution of extractable Fe(II) and Fe(III) concentrations. The estimated data, together with other information, may be useful for estimating microbial iron reduction potential [*Murray et al.*, 2001], and for aiding in estimation of bacterial transport parameters [*Fuller et al.*, 2000]. Although the statistical model is developed according to the data collected from a specific site for estimating solid Fe(II) and Fe(III) concentrations, the idea that geochemical parameters and geophysical attributes can be linked through their mutual dependence on physical and lithologic properties should be applicable for estimation of other geophysical parameters.

[45] We have shown that the developed method is effective for estimating geochemical parameters using the cross-validation method, but have not shown how the estimated results can improve the prediction of bacterial transport. Ideally, to evaluate the usefulness of the estimated geochemical heterogeneity for predicting bacterial transport, we should compare the prediction of bacterial transport using the estimated geochemical parameters to the one without using the geochemical data through a simulation model, and compare both the predictions with the results of bacterial transport experiments. However, modeling bacterial transport in subsurface itself is a topic of current research [e.g., *Murphy and Ginn*, 2000; *Sun et al.*, 2001; *Bhattacharjee et al.*, 2002; *Loveland et al.*, 2003]. The research requires a multidisciplinary effort, for example, understanding biogeochemical processes and the coupling of the processes with physical flow and transport, and mapping the spatial variability of field-scale physical and chemical properties in subsurface [*Smith et al.*, 1991; *Cozzarelli et al.*, 1999]. Although our study is part of the effort, it is not our intention to quantitatively show the usefulness of the estimated Fe(II) and Fe(III) concentrations for estimating bacterial transport parameters in the study.

[46] Our statistical model is developed based on regression analysis of multidimensional data at the South Oyster site. Similar to other estimation methods, the quality of the estimate is constrained by the quality and quantity of available direct measurements. In this study, we can only divide lithofacies into two statistically significant categories (sand and mud) based on analysis of the data we have. Within each category, Fe(II) and Fe(III) concentrations range over several orders of magnitudes, which result in associated uncertainty. However, our approach is general and not limited to two lithofacies. If we could collect more or higher-quality data that allow us to define more lithofacies, we could possibly obtain better estimates of Fe(II) and Fe(III) concentrations using the method.

Appendix A: Derivation of $[X_i|\cdot]$

[47] By substituting equations (3) and (4) into equation (8) and omitting all terms that are not directly related to X_i, we obtain $[X_i|\cdot]$ as follows:

$$\begin{aligned}
[X_i|\cdot] &\propto \exp\left\{-\frac{\tau_3}{2}(Y_i - r_1 - r_2X_i - r_3d_i)^2\right\} \\
&\quad \cdot \exp\left\{-\frac{\tau_2}{2}(X_i - v_1 - v_2L_i - v_3a_i - v_4L_ia_i)^2\right\} \\
&= \exp\left\{-\frac{\tau_3}{2}(r_2X_i - Y_i + r_1 + r_3d_i)^2\right\} \\
&\quad \cdot \exp\left\{-\frac{\tau_2}{2}(X_i - v_1 - v_2L_i - v_3a_i - v_4L_ia_i)^2\right\} \\
&\propto \exp\left\{-\frac{\tau_2 + r_2^2\tau_3}{2}X_i^2 + \tau_2(v_1 + v_2L_i + v_3a_i + v_4L_ia_i)X_i \right. \\
&\quad \left. + \tau_3r_2(Y_i - r_1 - r_3d_i)X_i\right\} \sim \text{Normal} \\
&\quad \left(\frac{\tau_2(v_1 + v_2L_i + v_3a_i + v_4L_ia_i) + r_2\tau_3(Y_i - r_1 - r_3d_i)}{\tau_2 + r_2^2\tau_3}, \tau_2 + r_2^2\tau_3\right),
\end{aligned} \tag{A1}$$

where v_1, v_2, v_3, v_4, r_1, r_2, r_3 are regression coefficients, τ_2 and τ_3 are the inverse variances, and Y_i, L_i, d_i, and a_i are the logarithmic Fe(III) concentration, lithofacies, depth, and logarithmic GPR attenuation at pixel i, respectively.

Appendix B: Indicator Kriging

[48] Let set A_i be the index set of the adjacent pixels of pixel i. Let p_s be the unconditional probability of observing sand at any pixel. The simple kriging mean μ_{pi} of observing sand is given by

$$\mu_{pi} = p_s + \sum_{j\in A_i}\lambda_j(L_j - p_s). \tag{B1}$$

The coefficients λ_j ($j\in A_i$) are determined by

$$\sum_{j\in A_i}\lambda_jC_{kj} = C_{ki}, \qquad k \in A_i, \tag{B2}$$

where C_{kj} and C_{ki} are the lithofacies covariances between pixel k and pixel j and between pixel k and pixel i, respectively. Both covariances are given by

$$C_{ij} = \sigma^2\exp\left\{-\sqrt{\left(\frac{\Delta x}{I_h}\right)^2 + \left(\frac{\Delta z}{I_v}\right)^2}\right\}, \tag{B3}$$

where σ^2 is a constant, which does not affect estimation of the coefficients, and Δx and Δz are the distances along horizontal and vertical directions between pixels i and j. I_v and I_h are the integral lengths along vertical and horizontal directions and derived from borehole data as

explained in section 2. To ensure $\mu_{pi} \in [0, 1]$, we let $p_i^* = \min\{1, \max\{0, \mu_{pi}\}\}$.

Appendix C: Derivation of $[L_i|\cdot]$

[49] By substituting equations (2) and (3) into equation (10) and using the identity $L_i^2 = L_i$, we obtain the full conditional probability of lithofacies as follows:

$$[L_i|\cdot] \sim \text{Bernoulli}(p), \tag{C1}$$

where

$$\begin{aligned} p &\propto [a_i|L_i][X_i|a_i, L_i]\left[L_i|L_j, j \in A_i\right] \\ &\propto \exp\{-0.5\tau_1(a_i - u_1 - u_2L_i)^2 - 0.5\tau_2(X_i - v_1 - v_2L_i - v_3a_i \\ &\quad - v_4L_ia_i)^2\}\{L_ip_i^* + (1 - L_i)(1 - p_i^*)\}. \\ &\propto \exp\{\tau_1u_2L_i(a_i - u_1 - 0.5u_2) + \tau_2(v_2 + v_4a_i)L_i(X_i - v_1 \\ &\quad - 0.5v_2 - v_3a_i - 0.5v_4a_i)\}\{L_ip_i^* + (1 - L_i)(1 - p_i^*)\}. \end{aligned} \tag{C2}$$

Normalization yields

$$p = \frac{p_i^*p_i}{1 - p_i^* + p_i^*p_i}, \tag{C3}$$

where

$$\begin{aligned} p_i = \exp\{&\tau_1u_2(a_i - u_1 - 0.5u_2) + \tau_2(v_2 + v_4a_i) \\ &(X_i - v_1 - 0.5v_2 - v_3a_i - 0.5v_4a_i)\}. \end{aligned} \tag{C4}$$

[50] **Acknowledgments.** Funding for this study was provided by the Department of Energy, Environmental Management Science Program and the Natural and Accelerated Bioremediation Research Program under grant DE-AC03-76SF00098, and by the National Science Foundation (NSF) under grant 0087802. The authors wish to thank John Peterson from Lawrence Berkeley National Laboratory for providing geophysical data and the Associate Editor and two anonymous reviewers for providing insightful comments and suggestions. All computations were carried out at the Center for Computational Seismology (CCS), supported by DOE's office of Basic Energy Science at the Lawrence Berkeley National Laboratory.

References

Bates, B. C., and E. P. Campbell (2001), A Markov Chain Monte Carlo scheme for parameter estimation and inference in conceptual rainfall-runoff modeling, *Water Resour. Res.*, *37*, 937–947.

Bernardo, J. M., and A. F. Smith (1994), *Bayesian Theory*, John Wiley, Hoboken, N. J.

Bhattacharjee, S., J. N. Ryan, and M. Elimelech (2002), Virus transport in physically and geochemically heterogeneous subsurface porous media, *J. Contam. Hydrol.*, *57*, 161–187.

Binley, A., and K. Beven (2003), Vadose zone flow model uncertainty as conditioned on geophysical data, *Ground Water*, *41*, 119–127.

Bosch, M. (1999), Lithologic tomography: From plural geophysical data to lithology estimation, *J. Geophys. Res.*, *104*, 749–766.

Bosch, M., A. Guillen, and P. Ledru (2001), Lithologic tomography: An application to geophysical data from the cadomian belt of northern Brittany, France, *Tectonophysics*, *31*, 197–227.

Canfield, D. E. (1989), Isotope fractionation by natural populations of sulfate-reducing bacteria, *Geochim. Cosmochim. Acta*, *65*, 1117–1124.

Chapelle, F. H. (2001), *Groundwater Microbiology and Geochemistry*, John Wiley, Hoboken, N. J.

Chen, J., and Y. Rubin (2003), An effective Bayesian model for lithofacies estimation using geophysical data, *Water Resour. Res.*, *39*(5), 1118, doi:10.1029/2002WR001666.

Chen, J., S. Hubbard, and Y. Rubin (2001), Estimating the hydraulic conductivity at the South Oyster site from geophysical tomographic data using Bayesian techniques based on the normal linear regression model, *Water Resour. Res.*, *37*, 1603–1613.

Cozzarelli, I. M., J. S. Herman, M. J. Baedecker, and J. M. Fischer (1999), Geochemical heterogeneity of a gasoline-contaminated aquifer, *J. Contam. Hydrol.*, *40*, 261–284.

Davis, J., and A. Annan (1989), Ground penetrating radar for high resolution mapping of soil and rock stratigraphy, *Geophys. Prospect*, *37*, 531–551.

DeFlaun, M. F., C. J. Murray, W. Holben, T. Scheibe, A. Mills, T. Ginn, T. Griffin, E. Majer, and J. L. Wilson (1997), Preliminary observations on bacterial transport in a coastal plain aquifer, *FEMS Microbiol. Rev.*, *20*, 473–487.

DeFlaun, M. F., et al. (2001), Breakthroughs in field-scale bacterial transport, *EOS Trans. AGU*, *82*(38), 417, 423–425.

Dong, H., T. C. Onstott, M. F. Deflaun, T. D. Scheibe, S. H. Streger, R. K. Rothmel, and B. J. Mailloux (2002), Relative dominance of physical versus chemical effects on the transport of adhesion-deficient bacteria in intact cores from South Oyster, Virgina, *Environ. Sci. Technol.*, *36*, 891–900.

Fuller, M. E., H. Dong, B. J. Mailloux, T. C. Onstott, and M. F. DeFlaun (2000), Examining bacterial transport in intact cores from Oyster, Virginia: Effect of sedimentary facies type on bacterial breakthrough and retention, *Water Resour. Res.*, *36*, 2417–2431.

Gelfand, A. E., and A. F. M. Smith (1990), Sampling-based approaches to calculating marginal densities, *J. Am. Stat. Assoc.*, *85*, 398–409.

Gelman, A., and D. B. Rubin (1992), Inference from iterative simulation using multiple sequences, *Stat. Sci.*, *7*, 457–472.

Geman, S., and D. Geman (1984), Stochastic relaxation, Gibbs distributions, and the Bayesian restoration of images, *IEEE Trans. Pattern Anal. Mach. Intel.*, *6*, 721–741.

Geweke, J. (1992), Evaluating the accuracy of sampling-based approaches to the calculation of posterior moments, in *Bayesian Statistics 4*, edited by J. M. Bernardo et al., pp. 169–193, Oxford Univ. Press, New York.

Gilks, W. R., S. Richardson, and D. J. Spiegelhalter (1996), *Markov Chain Monte Carlo in Practice*, Chapman and Hall, New York.

Hastings, W. K. (1970), Monte Carlo sampling methods using Markov chains and their applications, *Biometrika*, *87*, 97–109.

Hubbard, S., Y. Rubin, and E. Majer (1997), Ground penetrating radar-assisted saturation and permeability estimation in bimodal systems, *Water Resour. Res.*, *33*, 971–990.

Hubbard, S., J. Chen, J. Peterson, E. Major, K. Williams, D. J. Swift, B. Mailloux, and Y. Rubin (2001), Hydrogeological characterization of the South Oyster bacterial transport site using geophysical data, *Water Resour. Res.*, *37*, 2431–2456.

Johnson, W., et al. (2001), Ferrographic tracking of bacterial transport in the field at the narrow channel focus area, Oyster, Va, *Environ. Sci. Technol.*, *35*, 182–191.

Knapp, E. P., J. S. Herman, A. L. Mills, and G. M. Hornberger (2002), Changes in the sorption capacity of Coastal Plain sediments due to redox alteration of mineral surfaces, *Appl. Geochem.*, *17*, 387–398.

Loveland, J. P., S. Bhattacharjee, J. N. Ryan, and M. Elimelech (2003), Colloid transport in a geochemically heterogeneous porous medium: Aquifer tank experiment and modeling, *J. Contam. Hydrol.*, *65*, 161–182.

Mailloux, B. J., et al. (2003), The role of physical, chemical, and microbial heterogeneity on the field-scale transport and attachment of bacteria, *Water Resour. Res.*, *39*(6), 1142, doi:10.1029/2002WR001591.

Metropolis, N., A. W. Rosenbluth, M. N. Rosenbluth, A. H. Teller, and E. Teller (1953), Equations of state calculations by fast computing machines, *J. Chem. Phys.*, *21*, 1087–1091.

Michalak, A. M., and P. K. Kitanidis (2003), A method for enforcing parameter nonnegativity in Bayesian inverse problems with an application to contaminant source identification, *Water Resour. Res.*, *39*(2), 1033, doi:10.1029/2002WR001480.

Mills, A. L., J. S. Herman, G. M. Hornberger, and T. H. deJesus (1994), Effect of solution ionic strength and iron coatings on mineral grains on the sorption of bactreial cells to quartz sand, *Appl. Environ. Microbiol.*, *60*, 3600–3606.

Murphy, E. M., and T. R. Ginn (2000), Modeling microbial processes in porous media, *Hydrogeol. J.*, *8*, 142–158.

Murray, C. J., Y. L. Xie, E. E. Roden, and K. Overstreet (2001), Microbial iron reduction potential in Coastal Plain sediments, paper presented at the Annual Meeting, Geol. Soc. of Am., Boston, Mass.

Peterson, J. E. (2001), Pre-inversion processing and analysis of tomographic radar data, *J. Environ. Eng. Geophys.*, *6*, 1–18.

Peterson, J. E., B. N. Paulsson, and T. V. McEvilly (1985), Applications of algebraic reconstruction techniques to crosshole seismic data, *Geophysics*, *50*, 1566–1580.

Raftery, A. E., and S. Lewis (1992), How many iterations in the Gibbs sampler?, in *Bayesian Statistics 4*, edited by J. M. Bernardo et al., pp. 763–773, Oxford Univ. Press, New York.

Roden, E. E., and D. R. Lovely (1993), Evaluation of Fe-55 as a tracer of Fe (III) reduction in aquatic sediments, *Geomicrobiol. J.*, *11*, 49–56.

Rubin, Y. (2003), *Applied Stochastic Hydrology*, Oxford Univ. Press, New York.

Scheibe, T. D., and Y.-J. Chien (2003), An evaluation of conditioning data for solute transport prediction, *Ground Water*, *41*, 128–141.

Scholl, M. A., and R. W. Harvey (1992), Laboratory investigations on the role of sediment surface and groundwater chemistry in transport of bacteria through a contaminated sandy aquifer, *Environ. Sci. Technol.*, *26*, 1410–1417.

Smith, R. L., R. W. Harvey, and D. R. LeBlanc (1991), Importance of closely spaced vertical sampling in delineating chemical and microbiological gradients in groundwater studies, *J. Contam. Hydrol.*, *7*, 285–300.

Sun, N., M. Elimelech, N.-Z. Sun, and J. N. Ryan (2001), A novel two-dimensional model for colloid transport in physically and geochemically heterogeneous porous media, *J. Contam. Hydrol.*, *49*, 173–199.

Wildung, R. E., S. W. Li, C. J. Murray, K. M. Krupka, Y. Xie, N. J. Hess, and E. E. Roden (2004), Technetium reduction in sediments of shallow aquifer exhibiting dissimilatory iron reduction potential, *FEMS Microbiol. Ecol.*, *49*, 151–162.

J. Chen, S. Hubbard, and E. Majer, Lawrence Berkeley National Laboratory, MS 90-1116, 1 Cyclotron Road, Berkeley, CA 94720, USA. (jchen@lbl.gov; sshubbard@lbl.gov; elmajer@lbl.gov)

Y. Rubin, Department of Civil and Environmental Engineering, University of California, Berkeley, CA 94720, USA. (rubin@ce.berkeley.edu)

C. Murray, Pacific Northwest National Laboratory, P.O. Box 999, MS K6-81, Richmond, WA 99352, USA. (chris.murray@pnl.gov)

E. Roden, Department of Biological Sciences, University of Alabama, Tuscaloosa, AL 35487, USA. (eroden@bsc.as.ua.edu)